

Piezo-phototronic Effect in Centro-symmetric BiVO_4 Epitaxial Films

Pao-Wen Shao

National Chiao Tung University

Heng-Jui Liu

National Chung Hsing University

Yuanwei Sun

Peking University

Mei Wu

Peking University

Ren-Ci Peng

Xi'an Jiaotong University

Meng Wang

Tsinghua University

Fei Xue

The Pennsylvania State University

Xiaoxing Cheng

The Pennsylvania State University

Lei Su

University of California, Irvine

Hsiao-Wen Chen

National Taiwan Normal University

Meng-Chin Lin

National Tsing Hua University

Qian Zhuang

Westlake University

Jiawei Huang

Westlake University

Yachin Ivry

Israel Institute of Technology

Hsiang-Lin Liu

National Taiwan Normal University

Yu-Jung Lu

Academia Sinica

Shi Liu

Westlake University

Pu Yu

Tsinghua University

Long-Qing Chen

The Pennsylvania State University

Peng Gao

Peking University

Xiaoqing Pan

University of California, Irvine

Yung-Jung Hsu

National Chiao Tung University

Jyh-Ming Wu

National Tsing Hua University

Yi-Chun Chen

National Cheng Kung University

Ying-Hao Chu (✉ yhc@nctu.edu.tw)

National Chiao Tung University <https://orcid.org/0000-0002-3435-9084>

Article

Keywords: topology, non-polar ferroelastics, piezo-phototronic effect

Posted Date: February 18th, 2021

DOI: <https://doi.org/10.21203/rs.3.rs-200330/v1>

License:  This work is licensed under a Creative Commons Attribution 4.0 International License.

[Read Full License](#)

Abstract

With exciting functionality, topological defects in ferroic system have attracted much attention. Under proper design, the emergence of polar domain walls in non-polar ferroelastics enables piezo-phototronic effect. In this study, we revealed ferroelastic twin texture with localized piezoelectric effect in epitaxial BiVO_4 film by piezoresponse force microscopy. Supported by the strain field analysis, we found the piezoresponse confined at domain wall area is attributed to the flexoelectric effect induced by the presence of ferroelastic twin domains during the paraelastic to ferroelastic phase transition. The piezo-phototronic phenomenon was further supported the experimental evidence of dye-degradation and generation of reactive radicals. This work not only provides new insights into the introduction of piezo-phototronic effects in non-polar materials, but also sheds light on a new concept to use material inhomogeneity for acquiring multifunctionality.

Main Text

Multifunctional materials are desirable for next-generation electronic devices. They can be obtained through an utilization of mutual coupling among various kinds of physical mechanisms.¹ For example, the piezo-phototronic effect is a coupling of piezoelectric, semiconductor and photonic behaviors.²⁻⁵ For instance, imposing a strain to generate a piezo-potential can be used to control the carrier generation, transport, separation, and recombination in semiconductors for optoelectronic devices.^{6,7} Typically, such an effect occurs in materials with the break of centrosymmetry, classified as polar materials, setting up a criterion for material selection.⁸ However, inhomogeneity, such as topological defects, exists in materials and can possess symmetry and properties different from bulk materials.⁹ For example, ferroelectric/ferroelastic domain walls initially can display higher photoconductivity mainly because the photogenerated carriers are separated by a strong electric field to accumulate at domain wall region due to the symmetry breaking.^{10,11} So, the key question we want to address is: can the piezo-phototronic effect be triggered by proper design of inhomogeneity in materials with centrosymmetry? In this study, centrosymmetric BiVO_4 (BVO) is selected as a model system, because it is an attractive candidate for photoanode by virtue of its adequate bandgap (2.4–2.6 eV) and the advantages of non-toxicity and high stability.¹² Efforts on enhancing its performance were mostly focused on building up heterojunction for effective charge separation.^{13,14} Less attention was paid to the control and use of material inhomogeneity. In this work, we fabricated epitaxial BVO films on yttria-stabilized zirconia (YSZ) substrate. Due to the phase transition of BVO and metastable structure compatible with substrate, the formation of periodic domain patterns can be obtained. The temperature dependent ferroelasticity and corresponding domain structures of BVO film were probed to explore the phase transition and understand the origin of domain formation. The importance of BVO domain patterns was highlighted by spatial-resolved photoconductivity and photochemistry. We found that the flexoelectricity at domain walls in centro-symmetric BVO creates a piezo-potential to enhance photoelectrochemical performance. Our results not only launch a new research direction of piezo-phototronics, but also expand potential application of utilizing material inhomogeneity especially in photoelectrochemistry.

BVO exhibits ferroelasticity at room temperature with two energy degenerate states in crystal structure. They are two centro-symmetric space groups with different γ angle (i.e., the angle between a and b axis), 90.4° for I_2/b and 89.6° for I_2/a .^{15,16} One critical material inhomogeneity can be expected is the domain wall between these two structures. The properties of this inhomogeneity can be predicted by the first-principles density functional theory (DFT) calculations. We found that a spontaneous polarization arises at domain wall area, as depicted in Fig. 1a. In addition, Bi and V atoms at the interfaces between A/B domains are displaced oppositely with respect to their surrounding oxygen cages along the domain walls, respectively. (The detailed assumptions and quantified polarization are described in supplementary text S1 and Figs. 2.) Such results indicate the possibility that inhomogeneity induces polarization in centrosymmetric materials.¹⁷⁻¹⁹ Experimentally, these two degenerate states can be managed in epitaxial BVO film (monoclinic I_2/a , $a=5.204 \text{ \AA}$, $b=5.101 \text{ \AA}$, $c=11.69 \text{ \AA}$, $\gamma=89.6^\circ$) deposited on YSZ substrate (cubic, $a=5.153 \text{ \AA}$). The epitaxial relationship of BVO/YSZ was investigated by aberration-corrected scanning transmission electron microscopy (STEM) as shown in Figs. 6. The c-axis of BVO is parallel to that of YSZ, and there are two possible alignments of $[100]_{\text{BVO}} \parallel [100]_{\text{YSZ}}$ and $[010]_{\text{BVO}} \parallel [100]_{\text{YSZ}}$ for the in-plane conjunction. For simplicity, we sort them as A and B domains for a-axis and b-axis of BVO parallel to a-axis of YSZ, respectively. Because the lattice parameter (5.153 \AA) of YSZ is between those ($a=5.204 \text{ \AA}$ and $b=5.101 \text{ \AA}$) of BVO, either in-plane conjunction can be naturally stable. In Fig. 1b for A domains, I_2/b and I_2/a display different γ angles. Due to the combinations of two γ angles and two deviation angles (φ and 2φ , $\varphi=0.4^\circ$) from $[100]_{\text{YSZ}}$, there are four kinds of alignments for either A or B domains. Thus, by X-ray diffraction (XRD) reciprocal space mapping (RSM) (Fig. 1c), eight satellites could be systematically distinguished along YSZ (400) and around BVO (400). The detailed analysis is displayed in Figs. 7. A/B domains can be correlated to the periodic ferroelastic twin structures, which are clearly seen in plane-view STEM image taken along the zone axis of $[001]_{\text{YSZ}}$ in Fig. 1d. Figure 1e represents high-angle annular dark-field scanning transmission electron microscopy (HAADF)-STEM image and schematic lattices of A and B domains at $[001]_{\text{YSZ}}$ zone axis. The local domain is determined by comparing the fast Fourier transform (FFT) of both A and B domains in Figs. 8, and the diffraction pattern acquired in A domain region matches that received from B domain region if rotated by 90.37° ($1.07^\circ+89.3^\circ$) counterclockwise, indicating the two-fold symmetry. We hypothesize that the energy degenerate states of BVO as multiple domains create inhomogeneous distribution of spontaneous strain especially along in-plane direction due to the misfit between a and b axes of BVO. Thus, besides DFT calculation, the localized strain gradient at topological defects (i.e., domain walls) also suggests the possibility of inducing polarization through flexoelectricity.

Based on the inherent photoactivity of BVO, the emerging polarization at the domain wall implies the existence of the piezo-phototronic effect in our system. We further explore such a piezo-phototronic behavior by conducting rhodamine B (RhB) degradation experiments since dye degradation reaction could be driven by either solar energy or mechanical vibrational energy for photoactive semiconductors with piezoelectricity (inset in Fig. 1f).²⁰ Surprisingly, although monoclinic space groups (i.e., I_2/b and I_2/a) of BVO are centro-symmetric, we observed an outstanding piezo-catalytic performance even much higher

than its photo-catalytic activity in the thin film structure. Significantly, the rate constant (k) of piezo-phototronic effect is ~ 10 folds higher than that of photo-catalytic effect, as shown in Figs. 9 and table S1. Considering that the piezo-phototronic effect only occurs in piezoelectric materials, this unprecedented result inspires us to further investigate the mechanism of driving piezoresponse in centrosymmetric BVO and the critical role of domain patterns.

The coupling effect between domain pattern and polarization was verified experimentally with spatial resolution since twin domains in the BVO/YSZ heteroepitaxy (surface height in Fig. 2a) can be visualized through piezoresponse force microscopy (PFM). In-plane PFM phase signal in Fig. 2b reveals clear periodic contrast concentrating at domain walls, and it could be concluded that there are four directions of domains summarized in the inset of Fig. 2b. Moreover, the continuity of phase signal in each bundle domain^{21,22} suggests that the signal results from the in-plane piezoresponse, rather than the crosstalk of topography because the discontinuity on surface shows no signal. The line section of height and in-plane phase signal at one bundle domain are extracted to Fig. 2c, in which alternative A and B domains exist. Here we would like to emphasize the piezoresponse appeared at domain wall area with alternative phase value, and the visualization of in-plane piezoresponse vector fields is built by angle-resolved (AR) PFM in Figs. 10. The configuration of lattice transition at domain wall is illustrated in Fig. 2d. It represents that each bundle domain contains 180° head-to-head piezoresponse vector at neighboring domain walls, consistent with the DFT prediction (Unlike ferroelectrics, the direction of domain in Fig. 2b and flexo-polarity are unrelated to specific crystal axis due to the form of incommensurate domain wall.²³) However, the out-of-plane signal (in Figs. 11.) is negligible compared with the in-plane one. It is because in BVO, the strain gradient across domain wall area (calculated in supplementary text S2) lowers the local symmetry²⁴, and results in the piezoresponse mainly along in-plane direction, consistent with the structure correlation between A and B domains.

To further validate the flexoelectric effect and understand the role of domain walls with atomic-resolution, the visualization of strain field by the geometric phase analysis (GPA) was conducted. Fig. 2e shows the plane-view STEM image containing A and B domains, and as well as (220) facets in diffraction pattern (in Fig. 2f) were selected as g_1 and g_2 for analysis. Maps of the local shear strain field ($\epsilon_{xy} \sim 2\%$ in Fig. 2g) and lattice rotation ($\omega_{xy} \sim 1.2^\circ$ in Fig. 2h) are more pronounced compared with the normal strain fields (ϵ_{xx} and ϵ_{yy}) as shown in Figs. 12. Although the normal strain field is negligible, the evaluated shear strain gradient in Fig. 2i ($\sim 5 \times 10^6 \text{ m}^{-1}$) across the domain walls leads to the piezoresponse, which is also predicted by molecular dynamics simulations in previous study.²⁵ The direct observation of strain gradients is comparable with the calculated value ($\sim 4.23 \times 10^6 \text{ m}^{-1}$ in supplementary text S2), and such a strain gradient is an universal effect instead of occasional phenomenon since the in-plane strain gradient distributes throughout the film (cross-sectional STEM and GPA in Figs. 13). Furthermore, the neighboring domains walls represent opposite shear strain gradient, which is responsible for 180° head-to-head piezoresponse at neighboring domain walls in Fig. 2d. Combined with the domain width relationship with film thickness (Figs. 14), the universal strain distribution is due more to the material inhomogeneity rather than the substrate clamping effect (supplementary text S3). Based on the PFM, strain field analysis and

simulation results, the origin of flexoelectricity is believed to arise from the reduction of symmetry at domain wall area.

Given that the lattice misfit and the reduction of symmetry at domain walls give rise to the substantial strain gradients and result in piezo-response induced by the flexoelectric effect, the direct connection between ferroelastic and piezoelectric nature for BVO could be built by in-situ modulation of temperature, especially focusing on the phase transformation. When the temperature is above the Curie temperature of BVO,²⁶ ferroelastic monoclinic phase would transform into paraelastic tetragonal one. Due to the reduction of energy degeneracies in crystal structure, we expect the spontaneous strain would disappear as well. In Fig. 3a, when the temperature was increased to 135°C, the splitting satellites assemble in contrast to room temperature RSM (Fig. 1c), implying not only the expansion of b-axis, but also the contraction of a-axis in BVO. After the phase transformation at 325°C (Fig. 3b), the tetragonal diffraction spot of BVO (400) overlaps with that of YSZ (400), indicating a coherent heteroepitaxy ($a_{\text{BVO, tetragonal}} = a_{\text{YSZ, cubic}}$). Fig. 3c shows the change of lattice parameter with temperature. The lattice misfit between A and B domains could be calculated

$$(\text{misfit} = \frac{a_m - b_m}{a_m} = 2\%)$$

based on the lattice parameters of monoclinic phase of BVO. The lattice misfit also reduces to 0 after the phase transition. On the other hand, when it cools down to room temperature, the satellites appear as those initially observed (Figs. 15), featuring the reversibility of the phase transition. Furthermore, high temperature in-situ TEM and PFM²⁷ were carried out to gain insights into domain transformation. Plane-view TEM images in Figs. 16 reflect the transition temperature of ~275°C, and the strain relaxation process is mediated by the domain wall motion at 250°C. In agreement with the macroscopic phenomenon in the RSM results, the twin domain structure reappears after cooling down to room temperature. In-plane PFM signal at room temperature is shown in Fig. 3d (surface signal in Figs. 17). The inserted white curves mark the edge of bundle domain and in-plane domain distribution. The domain structure was then recorded at the temperature range from 25°C to 275°C (Figs. 18). Above the phase transition point of 275°C, the in-plane phase signal indeed disappears (in Fig. 3e). Moreover, in Fig. 3f, after cooling down to room temperature, the new-formed stripes of domain as well as the PFM signal appear again, featuring the generation of piezoresponse and its dependence on the phase transition. To understand the evolution of ferroelastic twin domains in BVO/YSZ heterostructure, the phase-field simulation was conducted, and the results are shown in Figs. 19. It also confirms that the distribution of multidomain with two perpendicular orientations arises from minimizing the total energy. From these results, we suggest that the formation of ferroelastic twin domains and the flexoelectricity inside twin domain wall are induced by the spontaneous strain during the tetragonal to monoclinic phase transition.

To examine the piezo-phototronic effect, we first consider it as a combination of piezo-catalytic and photo-catalytic processes. In Fig. 4a, the photo-catalytic effect mainly occurs inside BVO film, including

absorption of light, generation of photocarriers and transport of photocarriers.²⁸ On the other hand, the piezo-catalytic course relies on tuning surface screen charges, as illustrated in Fig. 4b. On the surface of twin domains, the piezopotential is balanced by screen charges. Due to the head-to-head polarization distribution, screen charges, i.e., e^- and h^+ , would accumulate on A and B domain area respectively. (The calculated piezoelectrically induced open-circuit voltage across each domain wall is ~ 0.25 mV. See details in supplementary text S4.) In aqueous solution, ultrasonic vibration creates a sinusoid function of hydraulic pressure, i.e., stress. Subsequently, the localized strain gradient and piezopotential at domain wall would also fluctuate with time to redistribute and release the screen charges from surface. As a consequence, the extra charges would spread into solution and serve as active charges. These free charge carriers further react with water and the dissolved oxygen, producing reactive oxygen species, e.g., $\cdot OH$ or $\cdot O_2^-$ radicals, for participation in the RhB degradation reaction.²⁹ (Detail description is in supplementary text S5.) To identify the reactive oxygen species responsible for piezo-catalytic reaction, the production of radicals is verified by the electron paramagnetic resonance (EPR) technique using 5,5-dimethyl-1-pyrroline N-oxide (DMPO) as spin scavenger. In Fig. 4c, the resonance peaks of DMPO $\cdot OH$ were detected, showing that $\cdot OH$ radicals were the main reactive species. Under darkness condition, $\cdot OH$ radicals could be generated by mechanical vibration stimuli and the concentration increases with vibration time. Under light illumination, the concentration of $\cdot OH$ radicals is further enhanced (Figs. 20), demonstrating the synergy between piezo-catalytic and photo-catalytic processes, which may account for the observed piezo-phototronic effect in Fig. 1f.

In order to prove the piezo-catalytic feature on BVO, $H Au Cl_4$ was introduced to conduct the deposition of Au nanoparticles on BVO. In the absence of reducing reagent and light illumination, $H Au Cl_4$ can be reduced to Au nanoparticles by reacting with radicals from piezo-catalytics.³⁰ As evidence from Fig. 4d, under mechanical vibration and darkness condition, an appreciable amount of Au nanoparticles was produced on BVO surface. Such a feature can be further corroborated by conducting the same Au deposition experiment on pure YSZ substrate, in which Au nanoparticles were barely produced (Figs. 21).

It should be noted that the piezo-catalytic feature can enhance the photo-catalytic efficiency of BVO by intrinsic in-plane piezopotential at domain walls. As illustrated in Fig. 4e, under light illumination, radicals generated from majority of charge carriers (i.e., electrons in n-type BVO) can reduce $H Au Cl_4$ to produced Au. Therefore, the deposition of Au nanoparticles would be prominent in the electron-rich domain. With antiparallel in-plane piezopotential at domain walls, the projected piezo-potential is from A to B domains (Fig. 2d) in each bundle domain. The majority charge carriers (i.e., electrons) would inevitably penetrate through domain wall and concentrate at B domains to dominate the photo-reduction reaction, whereas the minority charge carriers (i.e., holes) concentrate at A domains and show incapability for $H Au Cl_4$ reduction. As highlighted in Fig. 4f, the deposition of Au nanoparticles from photo-reduction reaction indeed shows domain selectivity on BVO surface. This outcome delivers the critical evidence that the piezopotential at domain walls can dominate the photo-reduction reaction on BVO because light harvesting efficiency (i.e., optical bandgap) of BVO remains the same regardless of the presence of domain walls (Figs. 22) The dominance of domain walls in the photo-reduction of $H Au Cl_4$ can be

examined by analyzing the periodicity of the deposited Au nanoparticles. As revealed in Figs. 23, the pattern of the deposited Au nanoparticles is morphologically consistent with domain width and the corresponding in-plane PFM signal, confirming that Au nanoparticles prefer to deposit at the areas of upper domains (B domain). With the increase of deposition time, instead of thoroughly covering the BVO surface, additional deposited Au tends to nucleate on the pre-formed nanoparticles. This observation suggested an effective electron transfer pathway from active B domains to the pre-formed Au nanoparticles (Figs. 21).

The behavior of carrier depletion at domain walls can be further explored by measuring the photoconductivity at BVO surface using conductive AFM. In Figs. 24, a significant enhancement in photoconductivity at domain regions can be observed. It is important to note here that the diffusion length of electron and holes in BVO are 70~200 nm³¹⁻³⁴, which is around three-folds larger than the twin domain width. This feature makes possible the effective separation of photo-generated electrons by the inherent electric field and their accumulation at specific upper domain area (B domain). Furthermore, the high density of twin domain walls also conduces to the suppression of charge carrier recombination of BVO for enhancing the photo-catalytic performance, which accounts for the observed piezo-phototronics effect as well. It is noteworthy that the key parameter to drive piezoresponse in centrosymmetric material is the strain gradient at domain wall. Based on this concept, we expect in other photo-active semiconductors with inhomogeneities at atomic scale, piezo-phototronics effect could be triggered regardless of the material category (e.g., epitaxial thin film or polycrystalline ceramics).

Conclusion

All in all, this study illustrates the engineering application of multifunctional topological defects and opens up opportunities for exploiting the piezo-phototronic effect based on centro-symmetric material. Ferroelastic twin domain feature of BVO was confirmed by XRD and TEM. Based on the in-plane PFM, GPA results and in-situ ferroelastic-paraelastic phase transition experiments, the strain gradient confined in domain walls along in-plane direction generates a piezopotential due to the flexoelectric effect. This piezopotential not only serves as a pathway for photogenerated carriers to accumulate at specific domain area under light illumination, but also holds promising engineering potentials for converting mechanical vibrational energy to chemical energy for photoelectrochemical applications. Our results demonstrate the predominant role of strain gradients at domain walls by flexoelectricity, and the localized piezopotential can be combined with the inherent photoactivity, lessening the gap for engineering the piezo-phototronic effect in centrosymmetric materials.

Declarations

Acknowledgments: This work is supported by Ministry of Science and Technology, Taiwan (grant No. MOST 106-2119-M-009-011-MY3, MOST 108-2628-E-009-006, MOST 106-2923-M-009-003-MY, MOST 109-2634-F-009-028) and the Center for Emergent Functional Matter Science of National Chiao Tung University from The Featured Areas Research Center Program within the framework of the Higher

Education Sprout Project by the Ministry of Education (MOE) in Taiwan. R.-C. P. acknowledges the support from Natural Science Foundation of China under grant number 51902247 and Natural Science Foundation of Shanxi Province under grant number 2020JQ-059. H.-L. L. acknowledges the support from Ministry of Science and Technology, Taiwan under grant number MOST 108-2112-M-003-013. P.G. acknowledges the support from the Key R&D Program of Guangdong Province (2018B030327001, 2018B010109009). Y. I. thanks the Zuckerman STEM Leadership Program as well as Ministry of Science and Technology, Israel, for financial support. Z. Q., J. H. and S. L. acknowledges the support from Westlake Education Foundation and the computational resource from Westlake University HPC Center.

Author contributions:

P.-W. S processed the sample growth and scanning probe microscopy and analyzed the data. H.-J.L. and Meng Wang processed the X-ray reciprocal mapping and resolved the phase transformation at elevated temperature. R.-C. P., F. X and X. C conducted the phase-field modeling. M.-C. L. processed the photodegradation, piezo-degradation and EPR measurement. Q. Z. and J. H. conducted the DFT calculations. Y. S. and Mei Wu acquired and analyzed the cross section TEM results. S. L. acquired the plane-view TEM results and resolved the phase transformation at elevated temperature. H.-W. C. acquired the bandgap results. Y. I. supervised the variable-temperature PFM and AFM work. Y.-C. C. provided guidance on PFM and CAFM data and related experiments. Y.-J. H. provided guidance on photodeposition results. P.-W. S and Y.-H. C conceived the idea, led the project, analyzed data, and co-wrote the paper. All the authors contributed to the manuscript.

Ethics declarations:

Competing interests: The authors declare no competing interests.

List of Supplementary Materials:

Materials and Methods

Supplementary Text S1 to S5

Figures S1-S24

References (35-48)

References

- 1 Tsymbal, E. Y., Dagotto, E. R. A., Eom, C. B. & Ramesh, R. *Multifunctional Oxide Heterostructures*. (OUP Oxford, 2012).
- 2 Liu, Y.-L. & Wu, J. M. Synergistically catalytic activities of BiFeO₃/TiO₂ core-shell nanocomposites for degradation of organic dye molecule through piezophototronic effect. *Nano Energy*

56, 74-81, doi:<https://doi.org/10.1016/j.nanoen.2018.11.028> (2019).

3 Zhu, L. & Wang, Z. L. Recent Progress in Piezo-Phototronic Effect Enhanced Solar Cells. *Adv. Funct. Mater.* **29**, 1808214, doi:<https://doi.org/10.1002/adfm.201808214> (2019).

4 Pan, C. *et al.* Progress in Piezo-Phototronic-Effect-Enhanced Light-Emitting Diodes and Pressure Imaging. *Adv. Mater.* **28**, 1535-1552, doi:<https://doi.org/10.1002/adma.201503500> (2016).

5 Pan, L. *et al.* Advances in Piezo-Phototronic Effect Enhanced Photocatalysis and Photoelectrocatalysis. *Adv. Energy Mater.* **10**, 2000214, doi:<https://doi.org/10.1002/aenm.202000214> (2020).

6 Zhang, X. *et al.* Enhanced optoelectronic performance of 3C-SiC/ZnO heterostructure photodetector based on Piezo-phototronic effect. *Nano Energy* **77**, 105119, doi:<https://doi.org/10.1016/j.nanoen.2020.105119> (2020).

7 Wang, X., Peng, D., Huang, B., Pan, C. & Wang, Z. L. Piezophotonic effect based on mechanoluminescent materials for advanced flexible optoelectronic applications. *Nano Energy* **55**, 389-400, doi:<https://doi.org/10.1016/j.nanoen.2018.11.014> (2019).

8 Wu, W. & Wang, Z. L. Piezotronics and piezo-phototronics for adaptive electronics and optoelectronics. *Nat. Rev. Mater.* **1**, 16031, doi:10.1038/natrevmats.2016.31 (2016).

9 Nataf, G. F. *et al.* Domain-wall engineering and topological defects in ferroelectric and ferroelastic materials. *Nat. Rev. Phys.* **2**, 634-648, doi:10.1038/s42254-020-0235-z (2020).

10 Vasudevan, R. K. *et al.* Field enhancement of electronic conductance at ferroelectric domain walls. *Nat. Commun.* **8**, 1318, doi:10.1038/s41467-017-01334-5 (2017).

11 Yang, S. Y. *et al.* Above-bandgap voltages from ferroelectric photovoltaic devices. *Nat. Nanotech.* **5**, 143-147, doi:10.1038/nnano.2009.451 (2010).

12 Zhang, L., Chen, D. & Jiao, X. Monoclinic Structured BiVO₄ Nanosheets: Hydrothermal Preparation, Formation Mechanism, and Coloristic and Photocatalytic Properties. *J. Phys. Chem. B* **110**, 2668-2673, doi:10.1021/jp056367d (2006).

13 Su, J., Guo, L., Bao, N. & Grimes, C. A. Nanostructured WO₃/BiVO₄ Heterojunction Films for Efficient Photoelectrochemical Water Splitting. *Nano Lett.* **11**, 1928-1933, doi:10.1021/nl2000743 (2011).

14 Rao, P. M. *et al.* Simultaneously Efficient Light Absorption and Charge Separation in WO₃/BiVO₄ Core/Shell Nanowire Photoanode for Photoelectrochemical Water Oxidation. *Nano Lett.* **14**, 1099-1105, doi:10.1021/nl500022z (2014).

- 15 Yeom, T. H., Choh, S. H., Song, K. J. & Jang, M. S. The domain structure of ferroelastic BiVO_4 studied by magnetic resonances. *J. Phys.: Condens. Matter* **6**, 383-392, doi:10.1088/0953-8984/6/2/010 (1994).
- 16 Choh, S. H. & Jang, M. S. Domain structure and magnetic resonance studies of ferroelastic BiVO_4 revisited. *Mater. Res. Express* **3**, 045021, doi:10.1088/2053-1591/3/4/045021 (2016).
- 17 Goncalves-Ferreira, L., Redfern, S., Artacho, E. & Salje, E. Ferrielectric Twin Walls in CaTiO_3 . *Phys. Rev. Lett.* **101**, 097602, doi:10.1103/PhysRevLett.101.097602 (2008).
- 18 Yokota, H. *et al.* Direct evidence of polar nature of ferroelastic twin boundaries in CaTiO_3 obtained by second harmonic generation microscope. *Phys. Rev. B* **89**, 144109, doi:10.1103/PhysRevB.89.144109 (2014).
- 19 Yokota, H., Matsumoto, S., Salje, E. K. H. & Uesu, Y. Symmetry and three-dimensional anisotropy of polar domain boundaries observed in ferroelastic LaAlO_3 in the complete absence of ferroelectric instability. *Phys. Rev. B* **98**, 104105, doi:10.1103/PhysRevB.98.104105 (2018).
- 20 Li, S. *et al.* Recent Advances of Ferro-, Piezo-, and Pyroelectric Nanomaterials for Catalytic Applications. *ACS Appl. Nano Mater.* **3**, 1063-1079, doi:10.1021/acsnm.0c00039 (2020).
- 21 Scott, J. F. *et al.* Superdomain dynamics in ferroelectric-ferroelastic films: Switching, jamming, and relaxation. *Appl. Phys. Rev.* **4**, 041104, doi:10.1063/1.5005994 (2017).
- 22 Ivry, Y., Chu, D. P. & Durkan, C. Bundles of polytwins as meta-elastic domains in the thin polycrystalline simple multi-ferroic system PZT. *Nanotechnology* **21**, 065702, doi:10.1088/0957-4484/21/6/065702 (2010).
- 23 Massad, J. E. & Smith, R. C. A Domain Wall Model for Hysteresis in Ferroelastic Materials. *J. Intell. Mater. Syst. Struct.* **14**, 455-471, doi:10.1177/1045389x03035235 (2003).
- 24 Zubko, P., Catalan, G., Buckley, A., Welche, P. R. L. & Scott, J. F. Strain-Gradient-Induced Polarization in SrTiO_3 Single Crystals. *Phys. Rev. Lett.* **99**, 167601, doi:10.1103/PhysRevLett.99.167601 (2007).
- 25 Salje, E. K. H., Li, S., Stengel, M., Gumbach, P. & Ding, X. Flexoelectricity and the polarity of complex ferroelastic twin patterns. *Phys. Rev. B* **94**, 024114, doi:10.1103/PhysRevB.94.024114 (2016).
- 26 David, W. I. F., Glazer, A. M. & Hewat, A. W. The structure and ferroelastic phase transition of BiVO_4 . *Phase Transit.* **1**, 155-169, doi:10.1080/01411597908213198 (1979).
- 27 Hershkovitz, A., Johann, F., Barzilay, M., Hendler Avidor, A. & Ivry, Y. Mesoscopic origin of ferroelectric-ferroelectric transition in BaTiO_3 : Orthorhombic-to-tetragonal domain evolution. *Acta Mater.*

187, 186-190, doi:<https://doi.org/10.1016/j.actamat.2020.01.051> (2020).

28 Ma, Y., Pendlebury, S. R., Reynal, A., Le Formal, F. & Durrant, J. R. Dynamics of photogenerated holes in undoped BiVO₄ photoanodes for solar water oxidation. *Chem. Sci.* **5**, 2964-2973, doi:10.1039/C4SC00469H (2014).

29 Wang, Y. *et al.* Piezo-catalysis for nondestructive tooth whitening. *Nat. Commun.* **11**, 1328, doi:10.1038/s41467-020-15015-3 (2020).

30 Frias Batista, L. M. *et al.* Kinetic Control of [AuCl₄]⁻ Photochemical Reduction and Gold Nanoparticle Size with Hydroxyl Radical Scavengers. *J. Phys. Chem. B* **123**, 7204-7213, doi:10.1021/acs.jpcc.9b04643 (2019).

31 Rettie, A. J. E. *et al.* Combined Charge Carrier Transport and Photoelectrochemical Characterization of BiVO₄ Single Crystals: Intrinsic Behavior of a Complex Metal Oxide. *J. Am. Chem. Soc.* **135**, 11389-11396, doi:10.1021/ja405550k (2013).

32 Abdi, F. F., Savenije, T. J., May, M. M., Dam, B. & van de Krol, R. The Origin of Slow Carrier Transport in BiVO₄ Thin Film Photoanodes: A Time-Resolved Microwave Conductivity Study. *J. Phys. Chem. Lett.* **4**, 2752-2757, doi:10.1021/jz4013257 (2013).

33 Song, J. *et al.* Tailoring Crystallographic Orientations to Substantially Enhance Charge Separation Efficiency in Anisotropic BiVO₄ Photoanodes. *ACS Catal.* **8**, 5952-5962, doi:10.1021/acscatal.8b00877 (2018).

34 Zhong, D. K., Choi, S. & Gamelin, D. R. Near-Complete Suppression of Surface Recombination in Solar Photoelectrolysis by "Co-Pi" Catalyst-Modified W:BiVO₄. *J. Am. Chem. Soc.* **133**, 18370-18377, doi:10.1021/ja207348x (2011).

Figures

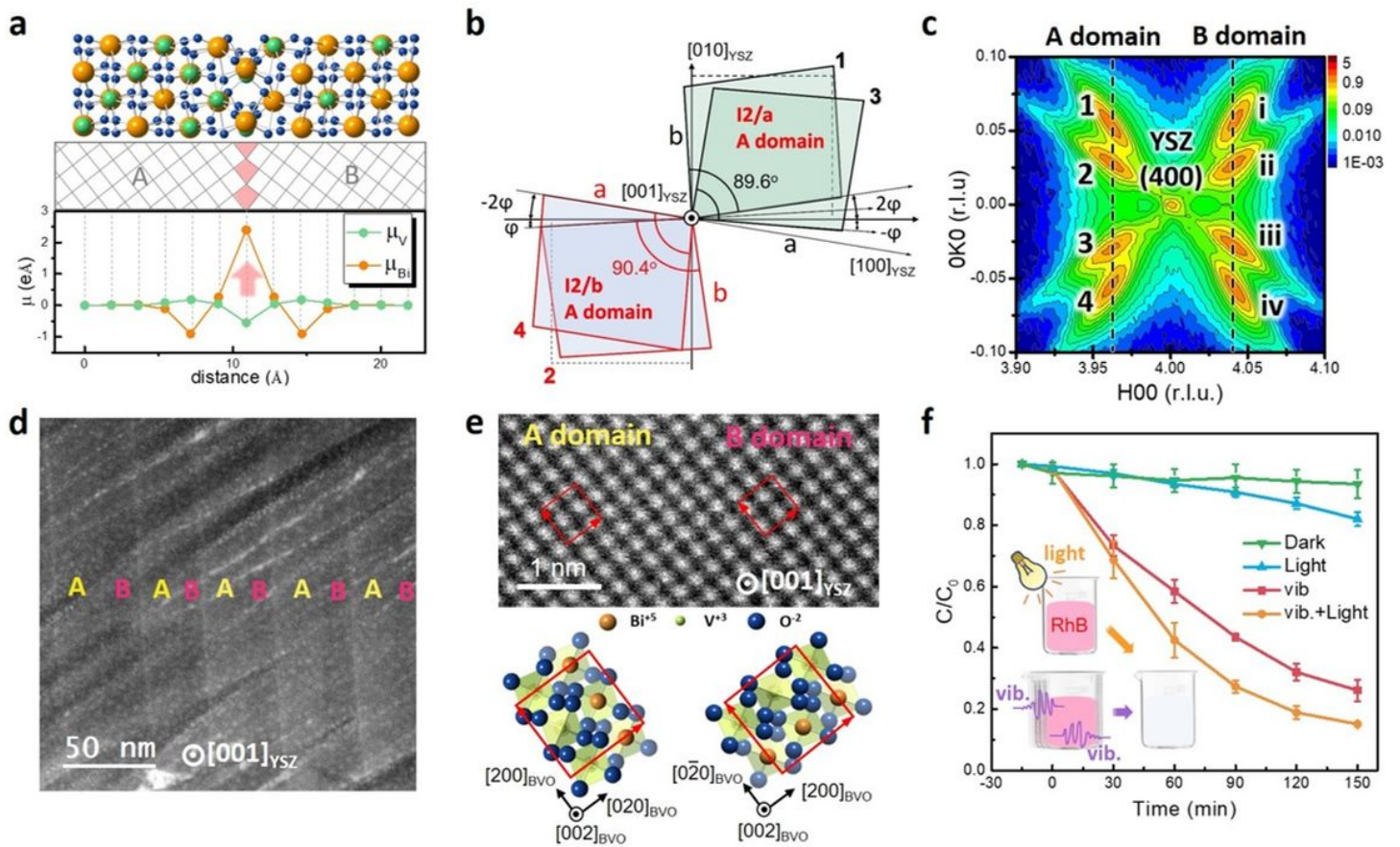


Figure 1

Characterization and piezo-phototronics of BVO film. a, DFT calculations of ferroelastic BVO structures. Local electrical dipoles centered at V and Bi atoms across the supercell containing A/B domain wall. The red arrows represent the net polarization. The green, orange, and blue atoms represent V, Bi, and O atoms. b, Schematic of the epitaxial relationships and the deviation angle φ from $[001]_{YSZ}$. c, In-plane RSM of BVO (400) with YSZ (400) reference for a 100-nm-thick film. d, Plane view HAADF-STEM image at the surface. Diagonal lines are the curtain effect from the FIB preparation procedure. e, High-resolution plane-view HAADF-STEM images taken along the $[001]_{YSZ}$. The red boxes represent monoclinic unit cells of A and B domains. f, Photo-degradation, piezo-degradation and piezo-phototronic degradation of RhB by BVO film.

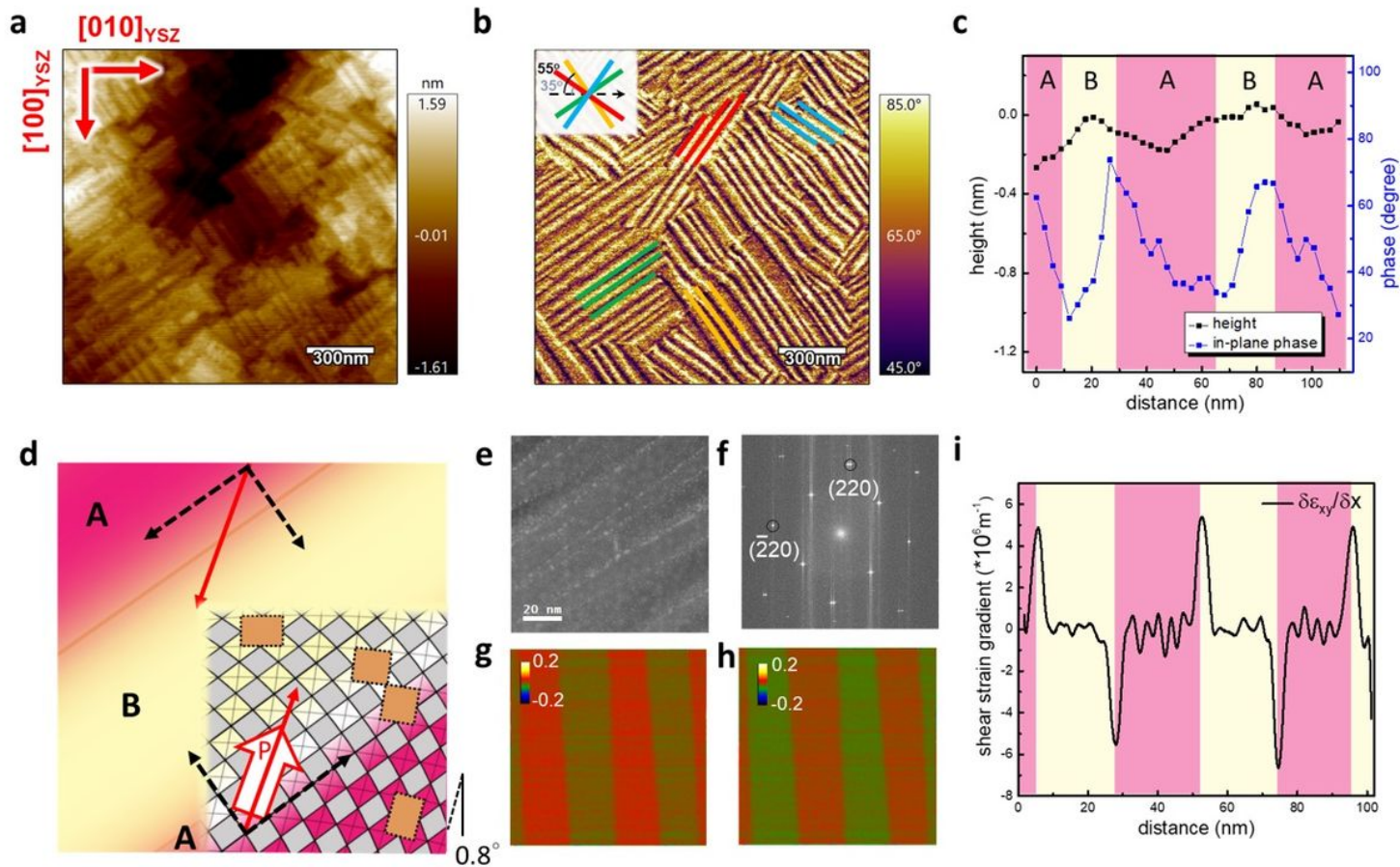


Figure 2

In-plane PFM and strain field characteristics. a, The topography of BVO/YSZ film. b, The according in-plane PFM phase signal recorded simultaneously. c, Line section extracted from a and b. d, The schematic distribution of piezoresponse direction. The detailed investigation of in-plane piezoresponse is in Figs. 10. e, STEM image. f, FFT of the area. The according g, $\delta\epsilon_{xy}$ and h, ω_{xy} . i, the shear strain gradient distribution along the direction almost perpendicular to the twin domain walls.

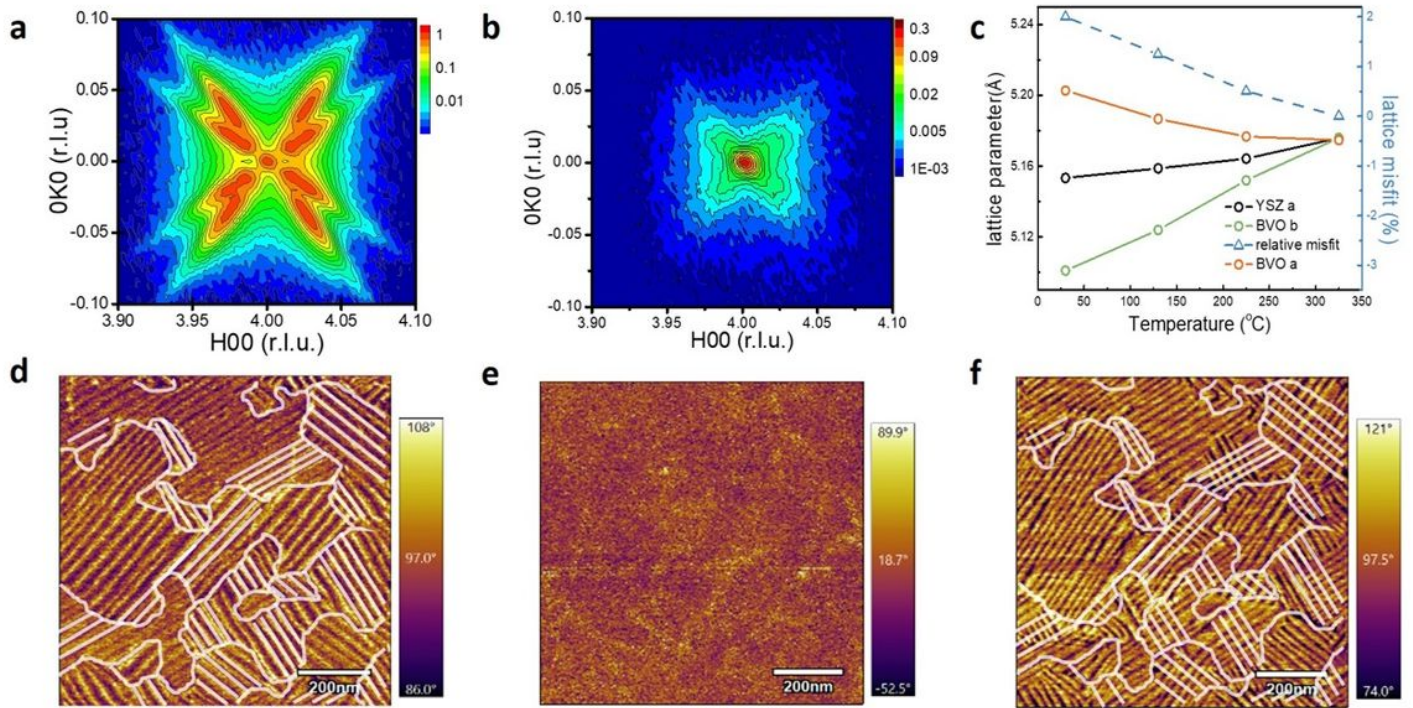


Figure 3

Temperature dependent characteristics of BVO/YSZ thin film. In-plane RSM of BVO (400) with YSZ (400) reference a, At 130°C. b, At 325°C. c, Variation of lattice parameters with temperature. The high temperature analysis of PFM: The in-plane phase signal of BVO d, at room temperature, e, at 275°C. f, after the heating process and cooling down to room temperature. For high temperature PFM analysis, these results were obtained at 1.5V ac tip bias, and we used single crystal diamond conducting probe due to its superior durability and stable resolution.

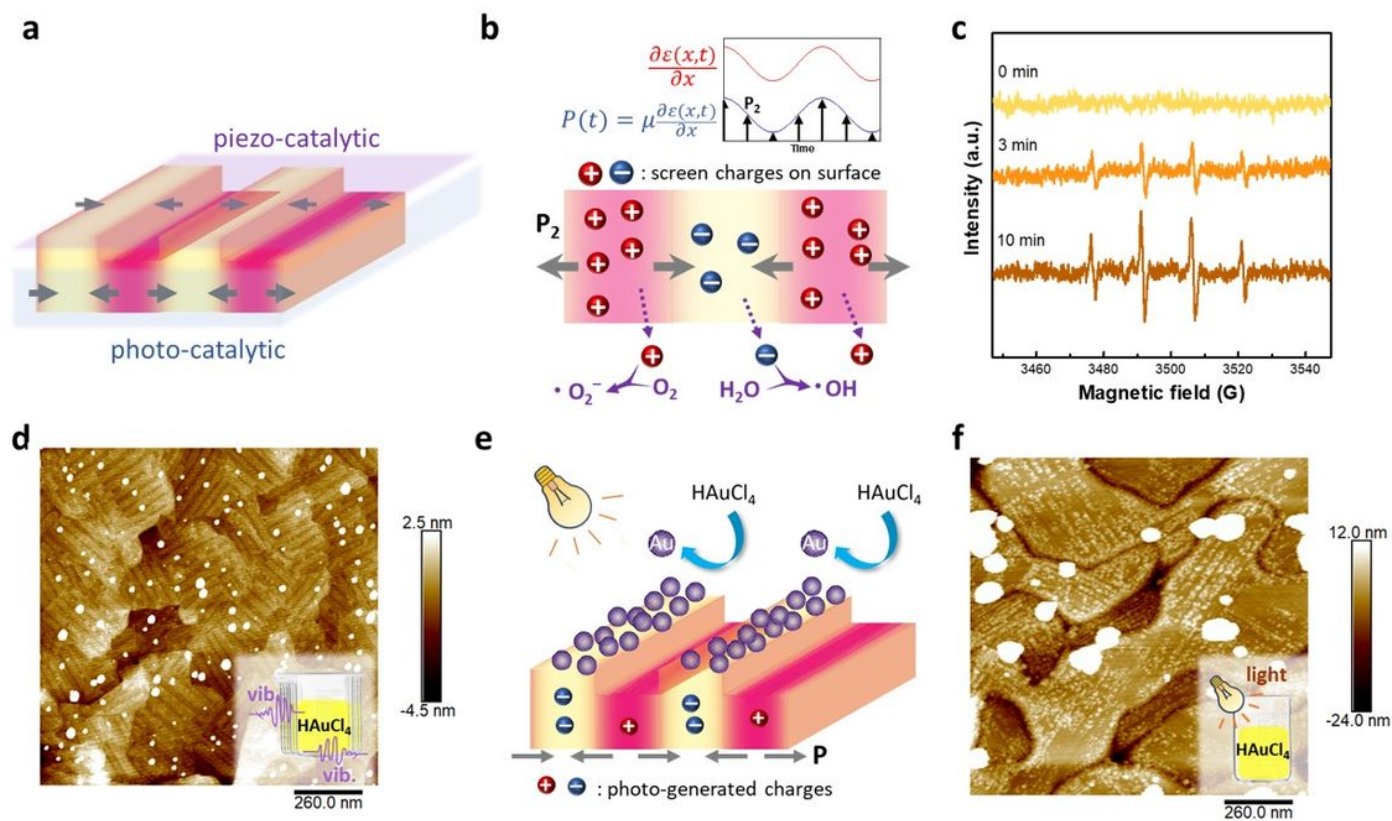


Figure 4

Effect of piezoresponse on the photoelectrochemistry of BVO. a, Schematic illustration of piezo-catalytic and photo-catalytic processes on BVO/YSZ. b, Plausible mechanism of piezo-catalytic effect. The black arrows represent the instant polarization with vibration stimuli. c, EPR spectra of DMPO·OH over BVO film in aqueous dispersion with vibration stimuli under dark condition. d, AFM image of BVO/YSZ after piezo-catalytic reduction of HAuCl₄. e, Schematic illustration of piezo-phototronic effect for domain-selective deposition of Au on BVO. f, AFM image of BVO/YSZ after piezo-phototronic reduction of HAuCl₄. The distribution also manifests four directions of twin domain patterns compared to Fig. 2b.

Supplementary Files

This is a list of supplementary files associated with this preprint. Click to download.

- [naturesupporting.docx](#)